

## Time-dependent QED approach to x-ray nonlinear Compton scattering


Dietrich Krebs,<sup>1,2,3</sup> David A. Reis,<sup>4</sup> and Robin Santra<sup>1,2,3,\*</sup>

<sup>1</sup>*Center for Free-Electron Laser Science, DESY, Notkestrasse 85, 22607 Hamburg, Germany*

<sup>2</sup>*Department of Physics, University of Hamburg, Jungiusstrasse 9, 20355 Hamburg, Germany*

<sup>3</sup>*The Hamburg Centre for Ultrafast Imaging, Luruper Chaussee 149, 22761 Hamburg, Germany*

<sup>4</sup>*Stanford PULSE Institute, SLAC National Accelerator Laboratory, Menlo Park, California 94025, USA*

 (Received 13 September 2017; revised manuscript received 21 May 2018; published 20 February 2019)

Motivated by a recent experiment [Fuchs *et al.*, *Nat. Phys.* **11**, 964 (2015)], we theoretically investigate the process of x-ray nonlinear Compton scattering (XNLC). Our approach is based on the time-dependent Schrödinger equation for an atomic system subject to an intense x-ray pulse, and explicitly accounts for the spontaneous scattering into a quantized photonic mode. We employ our framework to study multiple nonlinear scattering scenarios. Initially, we consider soft x rays at 500 eV photon energy to scatter nonlinearly off a helium target. For this, we find that XNLC is dominated by certain third-order processes rather than the naively expected mechanisms pertaining to the lowest order of perturbation theory. Subsequently, we apply our model to XNLC in helium at 4.0 keV photon energy and beryllium at 9.7 keV. Contrary to the conclusions drawn from the experimental observations, our results suggest a good agreement of the XNLC spectrum with simple, free-electron model predictions. Moreover, our studies reveal striking qualitative similarities of linear and nonlinear Compton scattering cross sections in this regime.

DOI: [10.1103/PhysRevA.99.022120](https://doi.org/10.1103/PhysRevA.99.022120)

### I. INTRODUCTION

Over the past decade, the advent of x-ray free-electron laser (FEL) sources [1–6] has opened up experimental opportunities at unprecedentedly high x-ray intensities (up to  $10^{20}$  W/cm<sup>2</sup>). This development has enabled numerous ground-breaking investigations that crucially rely on weak, linear signals (e.g., single molecule imaging [7]), yet moreover, it has uncovered a novel—namely the *nonlinear*—regime of x-ray-matter interaction [8–17].

Probing this regime at the Linac Coherent Light Source [4], a study by Fuchs *et al.* recently resulted in the observation of a nonlinear scattering signal, which was interpreted in terms of x-ray nonlinear Compton scattering (XNLC) [18]. In this process, two incoming x-ray photons nonsequentially interact with the target material (beryllium foil), being converted in the process into a single scattered photon at higher photon energy. Analogous to the case of regular Compton scattering, XNLC proceeds inelastically, i.e., it involves the transfer of energy onto a recoiling electron. This effect had previously been elusive in the x-ray regime, though its prediction dates back to 1963, when Kibble and Brown formulated their theoretical description of nonlinear Compton scattering for a free electron in strong electromagnetic fields [19]. Their findings notably include a relation between incoming ( $\omega_{\text{in}}$ ) and scattered ( $\omega_{\text{NLC}}$ ) photon energies:

$$\omega_{\text{NLC}} = \frac{n \omega_{\text{in}}}{1 + (n \alpha^2 \omega_{\text{in}})(1 - \cos \vartheta)}, \quad (1)$$

which parallels the well-known and -tested linear Compton kinematic [20,21], albeit for multiple ( $n$ ) incoming photons [22]. In printing Eq. (1), we employ the system of atomic units (a.u.) [23], which we adhere to throughout this article. Furthermore, we use  $\alpha$  ( $\approx 1/137$ ) to denote the fine-structure constant and  $\vartheta$  to denote the scattering angle.

Contrasting with Eq. (1), the experimentally observed spectrum from Ref. [18] exhibits systematically larger redshifts than predicted by the free-electron model for the XNLC process. This was interpreted as a breakdown of the free-electron approximation for bound-state contributions to XNLC [18]. In order to understand the redshift and verify its interpretation in terms of anomalous XNLC, the theoretical description of the process has to be improved beyond the free-electron case. Therefore, we aim to develop a description of XNLC that accounts both for the scattering process and the interaction with a binding potential.

Technically, this endeavor holds considerable challenges, as the conventional treatment of x-ray-matter interaction in terms of perturbation theory becomes “tremendously involved” [24] for nonlinear processes. This is due both to a rapidly increasing number of contributing terms and the intricacies arising from the description of intermediate states in a perturbative expansion. Moreover, any theoretical approach to XNLC is complicated by the necessity to account for nondipole effects owing to the short x-ray wavelength. Recent perturbative investigations of XNLC by Hopersky *et al.* [25], therefore, have been conducted only in the limit of several approximations regarding the above aspects. Most significantly, quoted work is restricted to the evaluation of a single contributing term pertaining to lowest order of perturbation theory (LOPT).

\*Corresponding author: robin.santra@cfel.de

Faced with the same difficulties, we decided to develop a nonperturbative approach for the theoretical investigation of (nonlinear) scattering phenomena. We base this approach on the explicit solution of the time-dependent Schrödinger equation (TDSE) in terms of propagating a wave-function ansatz that accounts both for the atomic system *and* the scattered photon—the latter in terms of a quantized photonic mode. This ansatz draws on our positive experiences with the time-dependent configuration-interaction singles (TDCIS) method [26–31], yet differs decidedly in its support for spontaneous emission or scattering into a nonparametric photon field. It is this time-dependent QED aspect that also sets our approach apart from most other wave-packet propagation schemes—with the notable exceptions of model studies by Grobe and co-workers [32–34], a strong field approach by Gonoskov and co-workers [35], and recent developments in quantum electrodynamical density-functional theory [36–38]. However, to the best of our knowledge, none of the aforementioned techniques have so far seen application to a realistic (three-dimensional) system. For this, we conduct our time-dependent QED simulations, investigating both regular (linear) Compton scattering and subsequently XNLC.

Choosing wave-packet propagation over conventional perturbative approaches provides us with a versatile model that can be applied to a variety of problems besides XNLC. Thereby, it offers otherwise unparalleled options for checks and benchmarks. Its versatility, however, comes at the price of considerable computational effort even for smaller systems. To meet this challenge, we base our model on an efficient partial discrete variable representation (DVR) and tailor its implementation to capitalize on the computing power of today’s graphics processing units (GPUs) [39].

The main body of our work below consists of Sec. II, wherein we introduce the foundations of our approach, and Sec. III, which contains three applications of our model to XNLC scenarios. We summarize our findings in Sec. IV. In addition, we provide appendixes that address details of the numerical implementation (Appendix A) and present validation of our model (Appendix B).

## II. THEORY

In order to describe XNLC at incoming photon energies of a few keV, we adopt a nonrelativistic description in terms of the TDSE:

$$i \frac{\partial}{\partial t} |\Psi\rangle = \hat{H} |\Psi\rangle. \quad (2)$$

This is well justified, as the energy transferred to an electron during XNLC by two photons is small compared to its rest energy of 511 keV [40].

In our investigation, we numerically solve Eq. (2) for an atomic system subject to an intense x-ray pulse and extract from its temporal evolution the probability for a spontaneous scattering event to occur. The TDSE describing such a scattering event may be pictured to resemble a two-level system:

$$i \frac{\partial}{\partial t} \begin{pmatrix} \beta(t) \\ \alpha(t) \end{pmatrix} = \begin{pmatrix} \hat{H}_{11} & \hat{H}_{1\uparrow} \\ \hat{H}_{\downarrow} & \hat{H}_{00} \end{pmatrix} \begin{pmatrix} \beta(t) \\ \alpha(t) \end{pmatrix}, \quad (3)$$

where the states represented by  $\alpha(t)$  exhibit no scattered photon, while those represented by  $\beta(t)$  do. Each set of states evolves under the influence of its pertaining Hamiltonian segment ( $\alpha(t)$ :  $\hat{H}_{00}$ ,  $\beta(t)$ :  $\hat{H}_{11}$ ) and is coupled to the other set by  $\hat{H}_{\uparrow}$  or  $\hat{H}_{\downarrow}$ , respectively, which mediates the creation or annihilation of a scattered photon.

In the following, we construct the constituents of the outlined model. In Sec. II A, we discuss the Hamiltonian that describes the coupled light-matter system, subsequently dedicating Sec. II B to the introduction of a suitable wave-function ansatz. In the course of this,  $\alpha(t)$  and  $\beta(t)$  are reintroduced as expansion coefficients. In Sec. II C, both elements are combined, recasting the TDSE into a set of coupled equations of motion (EOMs) for the expansion coefficients. At this point the Hamiltonian assumes a partitioning akin to Eq. (3). Finally in Sec. II D, we outline the relation of the simulation results to an experimentally accessible scattering cross section. For further details on the numerical implementation, we refer the reader to Appendix A.

### A. Hamiltonian

Within the framework of nonrelativistic QED [41,42] the most general Hamiltonian description of our setup may be written as

$$\hat{H} = \hat{H}_{\text{AT}} + \hat{H}_{\text{EM}} + \hat{H}_{\text{INT}}, \quad (4)$$

with  $\hat{H}_{\text{AT}}$  pertaining to the atomic system,  $\hat{H}_{\text{EM}}$  to the electromagnetic field, and  $\hat{H}_{\text{INT}}$  comprising the interaction of the two. The latter part accounts for—among other things—the scattering of photons by the atom and therefore is pivotal to our investigation. In order to incorporate its complexity into our model, and thus allow for an accurate description of XNLC, we, however, have to accept considerable simplifications with regard to the other components. Otherwise, we would find the challenging numerical calculations rendered completely unfeasible.

In our first step towards a solvable model, we approximate the atomic Hamiltonian  $\hat{H}_{\text{AT}}$ . Instead of treating its electron-electron interaction at full complexity, we resort to a simpler mean-field description in terms of the Hartree-Fock-Slater (HFS) model [43]. This approach has proven effective in numerous applications (see for example [44–47]) and provides us with a sensible approximation of the electronic structure of light atoms. The according Hamiltonian for  $N_{\text{elec}}$  electrons reads

$$\hat{H}_{\text{AT}} = \sum_{n=1}^{N_{\text{elec}}} \left( \frac{\hat{\mathbf{p}}_n^2}{2} + V_{\text{HFS}}(|\hat{\mathbf{r}}_n|) \right), \quad (5)$$

where  $\hat{\mathbf{p}}_n$  denotes the canonical momentum operator pertaining to the  $n$ th electron and  $\hat{\mathbf{r}}_n$  its position operator. The HFS potential in turn is marked by  $V_{\text{HFS}}(|\mathbf{r}|)$ .

Next, we consider the modeling of the electromagnetic field, encompassing both the incoming FEL pulse and the scattered photon. In describing the spontaneous creation of the latter, it is mandatory to account for the quantized nature of the field, whereas the description of the FEL radiation may well be accomplished classically [48]. Given the considerable computational facilitation yielded by a (partially) classical

treatment, we adopt a mixed description, writing the overall vector potential as the sum of the classical incoming pulse and a quantized part accounting for the scattered photon:

$$\hat{\mathbf{A}}(\mathbf{r}, t) = \mathbf{A}_{\text{in}}(\mathbf{r}, t) + \hat{\mathbf{A}}_q(\mathbf{r}). \quad (6)$$

Herein, we require both parts to satisfy the Coulomb gauge [ $\nabla \cdot \mathbf{A}(\mathbf{r}) = 0$ ] independently. We further choose the incoming pulse to be of a plane-wave nature, using a carrier frequency  $\omega_{\text{in}} = |\mathbf{k}_{\text{in}}|/\alpha$  that is modulated by a slowly varying pulse envelope  $A(t)$ :

$$\mathbf{A}_{\text{in}}(\mathbf{r}, t) = A(t) (\boldsymbol{\epsilon}_{\text{in}} e^{i(\mathbf{k}_{\text{in}} \cdot \mathbf{r} - \omega_{\text{in}} t)} + \text{H.c.}). \quad (7)$$

Here,  $\boldsymbol{\epsilon}_{\text{in}}$  is the complex unit vector marking the polarization of the pulse ( $\boldsymbol{\epsilon}_{\text{in}} \perp \mathbf{k}_{\text{in}}$ ) and the notation ‘‘H.c.’’ is used to indicate the Hermitian conjugate of the preceding term.

Regarding the quantized part of the field  $\hat{\mathbf{A}}_q(\mathbf{r})$ , we are left with the challenge to cover a large set of modes, into which the scattered photon could be emitted. In order to simplify this problem, we proceed in analogy to common perturbative scattering analyses, restricting our model to a single mode per calculation. Thereby, we significantly reduce the computational complexity of a simulation run, albeit at the expense of requiring multiple, successive calculations to scan a full spectrum [49]. The vector potential employed to represent the quantized field then reads

$$\hat{\mathbf{A}}_q(\mathbf{r}) = \sqrt{\frac{2\pi}{V\omega_q\alpha^2}} (\hat{a}_q \boldsymbol{\epsilon}_q e^{i\mathbf{k}_q \cdot \mathbf{r}} + \text{H.c.}), \quad (8)$$

where  $\hat{a}_q$  and  $\hat{a}_q^\dagger$  are the annihilation and creation operators, respectively, for a photon in the quantized mode (q). Its energy is given by  $\omega_q = |\mathbf{k}_q|/\alpha$ , while  $\boldsymbol{\epsilon}_q$  once again marks its polarization ( $\boldsymbol{\epsilon}_q \perp \mathbf{k}_q$ ). The quantization volume of the electromagnetic field (cf., e.g., Ref. [41]) enters the calculations in terms of  $V$ , however, it should be noted that all physical results are independent of its numerical value (cf. Sec. II D).

With the above setup in place,  $\hat{H}_{\text{EM}}$  concerns only the quantized mode (q) and therefore reads

$$\hat{H}_{\text{EM}} = \hat{n}_q \omega_q. \quad (9)$$

This expression is adjusted for the global energy offset caused by the vacuum contribution  $\omega_q/2$  and thus focuses only on the number of photons actually occupying the mode. The latter is counted by the number operator  $\hat{n}_q = \hat{a}_q^\dagger \hat{a}_q$ .

Based on the modeling of  $\hat{H}_{\text{AT}}$  and  $\hat{H}_{\text{EM}}$ , we can now introduce the light-matter interaction term without the need for further approximations. We adopt the principle of minimal coupling [50], rendering  $\hat{H}_{\text{INT}}$ :

$$\hat{H}_{\text{INT}} = \sum_{n=1}^{N_{\text{elec}}} \left( \alpha \hat{\mathbf{p}}_n \cdot \hat{\mathbf{A}}(\hat{\mathbf{r}}_n, t) + \frac{\alpha^2}{2} \hat{\mathbf{A}}^2(\hat{\mathbf{r}}_n, t) \right). \quad (10)$$

## B. Wave-function ansatz

The second decisive part of TDSE modeling concerns the formulation of a wave-function ansatz that spans a suitable space of states.

Regarding the atomic system, we hereunto adopt an expansion analogous to the TDCIS approach of Ref. [26], which has been shown to capture the physics of various atomic

phenomena [28,29,51]. In particular, we base our description on the HFS ground state  $|\Phi_0\rangle$  and additionally account for one-particle one-hole configurations  $|\Phi_i^a\rangle$ . The latter denote spin-symmetrized excitations [52] on top of  $|\Phi_0\rangle$ , in which an electron is (spatially) promoted from its initial orbital  $|\varphi_i\rangle$  into a previously unoccupied orbital  $|\varphi_a\rangle$ .

Besides the electronic configuration, the wave-function ansatz also has to account for the state of the photonic mode (q). To this end, each electronic state is paired with one of the two states of the photonic system, i.e.,  $|n_q\rangle = |0\rangle$  and  $|n_q\rangle = |1\rangle$ , representing the possible absence or presence of a scattered photon, respectively. Thus, our overall wave-function ansatz reads

$$|\Psi(t)\rangle = \alpha_0(t) |\Phi_0\rangle |0\rangle + \sum_{i,a} \alpha_i^a(t) |\Phi_i^a\rangle |0\rangle + \beta_0(t) |\Phi_0\rangle |1\rangle + \sum_{j,b} \beta_j^b(t) |\Phi_j^b\rangle |1\rangle, \quad (11)$$

wherein the structure of the two-level system of Eq. (3) is reflected. Note that the summation indices of the above ansatz implicitly relate to the underlying HFS orbitals  $|\varphi_p\rangle$ , for which we adhere to the following convention: Indices  $i, j, k$ , and  $l$  are taken to refer to initially occupied orbitals, whereas indices  $a, b, c$ , and  $d$  remain reserved for their unoccupied (virtual) counterparts.

All single-particle orbitals  $|\varphi_p\rangle$ —regardless of their indices—are solutions of the self-consistent HFS equation,

$$\left( \frac{\hat{\mathbf{p}}^2}{2} + V_{\text{HFS}}(|\hat{\mathbf{r}}|) \right) |\varphi_p\rangle = \varepsilon_p |\varphi_p\rangle, \quad (12)$$

with the spatial representation

$$\varphi_p(\mathbf{r}) = \frac{u_{n_p l_p}(|\mathbf{r}|)}{|\mathbf{r}|} Y_{l_p m_p}(\Omega_{\mathbf{r}}). \quad (13)$$

Herein,  $u_{n_p l_p}(|\mathbf{r}|)$  marks the radial part of the orbital wave function, while its angular component is represented by the spherical harmonic  $Y_{l_p m_p}(\Omega_{\mathbf{r}})$ .

## C. Equations of motion

With both the Hamiltonian  $\hat{H}$  and the wave-function ansatz  $|\Psi(t)\rangle$  outlined, we proceed to recast the TDSE [Eq. (2)] into equations of motion (EOMs) for the expansion coefficients  $\alpha_0(t)$ ,  $\beta_0(t)$ ,  $\alpha_i^a(t)$ , and  $\beta_j^b(t)$ . To this end, we project the assembled TDSE of our model onto the various constituent states of the ansatz given in Eq. (11).

Any electronic matrix element that occurs in this process can subsequently be simplified using the Slater-Condon rules:

$$\langle \Phi_0 | \hat{H} | \Phi_0 \rangle = 2 \sum_j \langle \varphi_j | \hat{H} | \varphi_j \rangle =: 2 \langle \hat{H} \rangle_{\text{occ}}, \quad (14)$$

$$\langle \Phi_0 | \hat{H} | \Phi_i^a \rangle = \sqrt{2} \langle \varphi_i | \hat{H} | \varphi_a \rangle, \quad (15)$$

$$\langle \Phi_k^c | \hat{H} | \Phi_i^a \rangle = \delta_{ik} \langle \varphi_c | \hat{H} | \varphi_a \rangle - \delta_{ac} \langle \varphi_i | \hat{H} | \varphi_k \rangle + \delta_{ik} \delta_{ac} 2 \langle \hat{H} \rangle_{\text{occ}}, \quad (16)$$

in which  $\delta_{ik}$  denotes the Kronecker symbol and the trace over initially occupied orbitals  $\langle \dots \rangle_{\text{occ}}$  is introduced to improve

readability. Note that on the right-hand side of Eqs. (14)–(16) the operator  $\hat{H}$  is understood to act only on a single electron.

Following the above rules, the EOMs written in terms of the HFS orbitals read

$$i \frac{\partial}{\partial t} \alpha_0 = 2 \alpha_0 \langle \hat{H}_{00} \rangle_{\text{occ}} + \sqrt{2} \sum_{i,a} \alpha_i^a \langle \varphi_i | \hat{H}_{00} | \varphi_a \rangle + 2 \beta_0 \langle \hat{H} \downarrow \rangle_{\text{occ}} + \sqrt{2} \sum_{j,b} \beta_j^b \langle \varphi_j | \hat{H} \downarrow | \varphi_b \rangle, \quad (17)$$

$$i \frac{\partial}{\partial t} \alpha_k^c = 2 \alpha_k^c \langle \hat{H}_{00} \rangle_{\text{occ}} + \sqrt{2} \alpha_0 \langle \varphi_c | \hat{H}_{00} | \varphi_k \rangle - \sum_i \alpha_i^c \langle \varphi_i | \hat{H}_{00} | \varphi_k \rangle + \sum_a \alpha_a^c \langle \varphi_c | \hat{H}_{00} | \varphi_a \rangle + 2 \beta_k^c \langle \hat{H} \downarrow \rangle_{\text{occ}} + \sqrt{2} \beta_0 \langle \varphi_c | \hat{H} \downarrow | \varphi_k \rangle - \sum_j \beta_j^c \langle \varphi_j | \hat{H} \downarrow | \varphi_k \rangle + \sum_b \beta_b^c \langle \varphi_c | \hat{H} \downarrow | \varphi_b \rangle, \quad (18)$$

$$i \frac{\partial}{\partial t} \beta_0 = 2 \alpha_0 \langle \hat{H} \uparrow \rangle_{\text{occ}} + \sqrt{2} \sum_{i,a} \alpha_i^a \langle \varphi_i | \hat{H} \uparrow | \varphi_a \rangle + 2 \beta_0 \langle \hat{H}_{11} \rangle_{\text{occ}} + \sqrt{2} \sum_{j,b} \beta_j^b \langle \varphi_j | \hat{H}_{11} | \varphi_b \rangle, \quad (19)$$

$$i \frac{\partial}{\partial t} \beta_k^c = 2 \alpha_k^c \langle \hat{H} \uparrow \rangle_{\text{occ}} + \sqrt{2} \alpha_0 \langle \varphi_c | \hat{H} \uparrow | \varphi_k \rangle - \sum_i \alpha_i^c \langle \varphi_i | \hat{H} \uparrow | \varphi_k \rangle + \sum_a \alpha_a^c \langle \varphi_c | \hat{H} \uparrow | \varphi_a \rangle + 2 \beta_k^c \langle \hat{H}_{11} \rangle_{\text{occ}} + \sqrt{2} \beta_0 \langle \varphi_c | \hat{H}_{11} | \varphi_k \rangle - \sum_j \beta_j^c \langle \varphi_j | \hat{H}_{11} | \varphi_k \rangle + \sum_b \beta_b^c \langle \varphi_c | \hat{H}_{11} | \varphi_b \rangle, \quad (20)$$

where we omit to carry the time dependence of the expansion coefficients in favor of visual clarity.

More importantly, we choose to partition the single-particle Hamiltonian in a way that reflects the two-level nature of the quantized photonic system [cf. Eq. (3)]. To this end, we collect all terms which act solely on the lower level ( $n_q = 0$ ) into the  $\hat{H}_{00}$  block, while the  $\hat{H}_{11}$  part pertains to the upper level ( $n_q = 1$ ) in an analogous way. Furthermore, we compile all operators that mediate transitions between the two levels into either  $\hat{H} \uparrow$  or  $\hat{H} \downarrow$ , which refer to the creation of a scattered photon or its annihilation, respectively.

Looking at each of these blocks in detail [53], we can identify different contributing processes, which we print alongside their diagrammatic representation for illustration:

$$\hat{H}_{00} = \frac{\hat{\mathbf{p}}^2}{2} + V_{\text{HFS}}(|\hat{\mathbf{r}}|) + \alpha A(t) \hat{\mathbf{p}} \cdot (\epsilon_{\text{in}} e^{i(\mathbf{k}_{\text{in}} \cdot \mathbf{r} - \omega_{\text{in}} t)} + \epsilon_{\text{in}}^* e^{-i(\mathbf{k}_{\text{in}} \cdot \mathbf{r} - \omega_{\text{in}} t)}) + \alpha^2 A(t)^2 + \frac{\alpha^2}{2} A(t)^2 ((\epsilon_{\text{in}})^2 e^{i2(\mathbf{k}_{\text{in}} \cdot \mathbf{r} - \omega_{\text{in}} t)} + (\epsilon_{\text{in}}^*)^2 e^{-i2(\mathbf{k}_{\text{in}} \cdot \mathbf{r} - \omega_{\text{in}} t)}) \quad (21)$$

$$\hat{H}_{11} = \frac{2\pi}{V\omega_q} + \hat{H}_{00} + \frac{\omega_q}{N_{\text{elec}}} \quad (22)$$

$$\hat{H} \uparrow = \sqrt{\frac{2\pi}{V\omega_q}} \hat{\mathbf{p}} \cdot \epsilon_q^* e^{-i\mathbf{k}_q \cdot \mathbf{r}} + \alpha \sqrt{\frac{2\pi}{V\omega_q}} A(t) ((\epsilon_q^* \cdot \epsilon_{\text{in}}) e^{-i((\mathbf{k}_q - \mathbf{k}_{\text{in}}) \cdot \mathbf{r} + \omega_{\text{in}} t)} + (\epsilon_q^* \cdot \epsilon_{\text{in}}^*) e^{-i((\mathbf{k}_q + \mathbf{k}_{\text{in}}) \cdot \mathbf{r} - \omega_{\text{in}} t)}) \quad (23)$$

$$\hat{H} \downarrow = (\hat{H} \uparrow)^\dagger. \quad (24)$$

Here, we employ red wiggly lines (thick) to symbolize interaction with the classical field and blue wiggly lines (thin) to depict interactions with the quantized mode (q).

Knowledge of the contributions shown above consequently allows us to investigate the mechanisms underlying XNLC. To this end, we may modify the propagation of the EOM by

selectively switching on or off contributing processes, based on Eqs. (21)–(24).

#### D. Evaluation of scattering

Implementing the presented model, we are—in principle—in a position to simulate various scattering scenarios. The

remaining task is to prescribe appropriate initial conditions to each simulation run and relate the propagated outcome to an overall scattering probability.

Both aspects are complicated in comparison to conventional atomic TDSE simulations (e.g., photoabsorption studies [29]) by the fact that there is permanent coupling among the light and matter subsystems. This particular coupling to the quantized mode (q) is mediated via the terms [cf. Eqs. (23) and (24)]:


(25)

and manifests itself as the virtual emission and reabsorption of a photon, i.e., the Lamb effect [54,55].

In this context, the ground state of the uncoupled system ( $|\Phi_0\rangle|0\rangle$ ) is no longer stationary and should not be chosen as the starting point of a scattering simulation. Instead, we choose to converge the coupled system to its true ground state prior to each simulation run by performing a (pre)propagation in imaginary time (cf., e.g., [56,57]). Thereby, the coupled system acquires a permanent population share in the one-photon sector, on top of which the real scattering process—driven by  $\mathbf{A}_{\text{in}}(\mathbf{r}, t)$ —induces further population transfer.

In order to distinguish the two contributions and count only the latter towards the scattering probability, we discriminate based on the physical response of the coupled system. While the ground state's population in the one-photon sector is necessarily bound, its scattering-induced counterpart corresponds to an ionized electronic wave packet (provided  $2\omega_{\text{in}} - \omega_{\text{q}} > \text{IP}$ ). Thus, by observing the outgoing flux of the wave function, we are able to obtain the probability  $P_{\text{q}}$  for Compton-like scattering in each simulation run (see also Appendix A 2).

Based on  $P_{\text{q}}$ , we formulate the (generalized) double differential scattering cross section (DDSCS) for XNLC:

$$\frac{d^2\sigma^{(2)}}{d\Omega_{\text{q}} d\omega_{\text{q}}} = \frac{V}{(2\pi)^3} \alpha^3 \omega_{\text{q}}^2 \frac{P_{\text{q}}}{F_{\text{in}}^{(2)}}. \quad (26)$$

Herein, we account for the nonlinear dependence of XNLC on the incoming field (cf. findings by Ref. [18]), by normalizing by the second-order nonlinear fluence  $F_{\text{in}}^{(2)}$ :

$$F_{\text{in}}^{(2)} = \int_0^{t_{\text{end}}} dt [J_{\text{in}}(t)]^2 = \int_0^{t_{\text{end}}} dt \frac{\alpha^2 \omega_{\text{in}}^2}{(2\pi)^2} [A(t)]^4. \quad (27)$$

Finally, note that the conversion prefactor of Eq. (26), includes the quantization volume  $V$  explicitly, which compensates for the implicit dependence on  $V$  carried by  $P_{\text{q}}$ . Thus, the resultant DDSCS is rendered independent of the particular numerical choice of  $V$ .

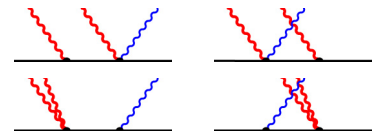
### III. APPLICATIONS

Once our XNLC model is implemented, we pursue two lines of applications: The first is concerned with the numerical reproduction of well-known phenomena in order to validate the functioning of our model (for details on this, see Appendix B). The second line, on the other hand, is dedicated to the actual study of nonlinear scattering processes. Focusing here on the latter, we investigate three cases of XNLC in the following subsection. In Sec. III A, we report

on XNLC in helium for comparatively low photon energies [ $\omega_{\text{in}} = 18.37$  a.u. ( $\approx 500$  eV)], addressing in this scenario the previous work of Hopersky *et al.* [25], whereas in Secs. III B and III C we consider XNLC at higher energies in an effort to retrace the experimental observations by Fuchs *et al.* [18]. These sections concern XNLC in helium at  $\omega_{\text{in}} = 147$  a.u. ( $\approx 4.0$  keV) and XNLC in beryllium at  $\omega_{\text{in}} = 358$  a.u. ( $\approx 9.7$  keV), respectively.

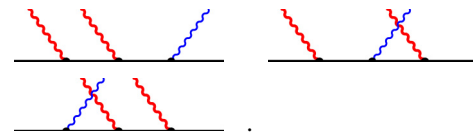
#### A. XNLC in helium at 500 eV

The first application of our XNLC program to nonlinear scattering concerns a scenario previously investigated by Hopersky *et al.* [25]. In quoted work, the authors conduct a perturbative analysis of nonlinear scattering in helium for incoming photon energies of 500 eV. They restrict their treatment to lowest order of perturbation theory (LOPT), considering initially the diagrammatic contributions:


(28)

Subsequently, they reduce the above set by argument to the first term only.

Overall, this ansatz appears problematic to us, as it neglects contributions of the fully  $\hat{\mathbf{p}} \cdot \hat{\mathbf{A}}$ -type diagrams:


(29)

While these expressions indeed do not pertain to LOPT, they nevertheless exhibit the same order of interaction strength ( $\alpha^3$ ) as the terms implied by the diagrams (28). Therefore, it seems unjustified to ignore them *a priori*.

In the following, we employ our nonperturbative approach—partly truncated—to investigate the importance of these additional contributions and thereby test the adequacy of the LOPT ansatz. In all of these calculations, we ensure that our results remain comparable to perturbation theory in general, by choosing the applied field well within the perturbative (multiphoton) regime. Specifically, we conduct all investigations using Gaussian pulses with a maximum pulse envelope of  $A(t_{\text{max}}) = 0.5$  a.u. [58].


As a first step, we attempt to simulate the behavior of the restricted scattering mechanism employed by Ref. [25]:


(30)

To this end, we disable the vertices


(31)

within the Hamiltonian segments  $\hat{H}\uparrow$  and  $\hat{H}\downarrow$  [Eqs. ((23), (24))] of our model, which then allows for nonlinear scattering only through


(32)

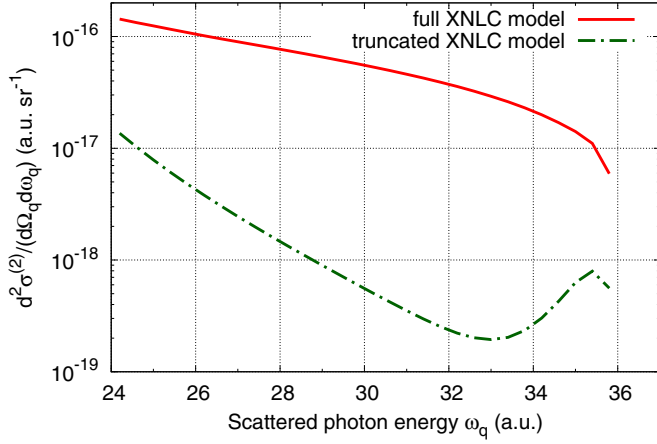


FIG. 1. The DDSCS for nonlinear Compton scattering at  $\omega_{\text{in}} = 18.37$  a.u. ( $\approx 500$  eV) calculated both with the truncated XNLC model (green dash-dotted line) and its full implementation (red solid line).

to lowest order. This gives the closest representation of Ref. [25] within our model, as we cannot control the time ordering of the contributions. In our simulations, we reproduce the scattering geometry employed by Hopersky *et al.*, fixing a scattering angle of  $\vartheta = \pi/2$  with both fields polarized perpendicular to the scattering plane.

The DDSCS that we extract from these calculations is plotted as the “truncated model” (green dash-dotted line) in Fig. 1 [59].

The cross section obtained from the truncated model exhibits a peak at the upper edge of the spectrum ( $\omega_q \approx 2\omega_{\text{in}} - IP$ ), which is reminiscent of the linear scattering case. Passing through a minimum at  $\omega_q \approx 33$  a.u., it then rises steeply towards lower scattered photon energies ( $\omega_q \rightarrow \omega_{\text{in}}$ ).

In contrast, employing the full model, i.e., enabling all terms of the Hamiltonian  $\hat{H}\uparrow$  and  $\hat{H}\downarrow$  in our simulations, we find a distinctly different result (red solid line). The according scattering signal features no peaked structure, but rises smoothly from its value at the upper edge ( $\omega_q \approx 2\omega_{\text{in}} - IP$ ) towards smaller  $\omega_q$ . Apart from this qualitative difference, there is also a striking disparity in the strength of both signals, with the full model dominating by approximately two orders of magnitude.

These findings strongly suggest that the restricted description in terms of the truncated model and—by extension—the treatment of Ref. [25] are insufficient to capture XNLC at the present photon energies.

Regarding the mechanism ultimately responsible for the disparity, it should be noted that further analyses, e.g., by disabling the vertices

$$(33)$$

in  $\hat{H}_{00}$  (and  $\hat{H}_{11}$ , respectively), which suppresses the XNLC contributions

$$(34)$$

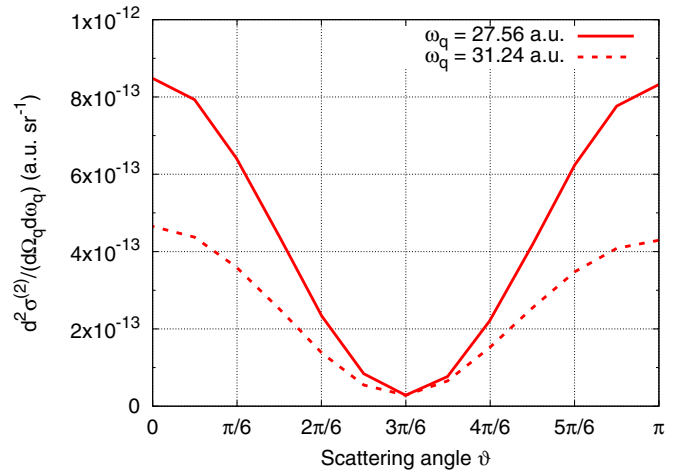


FIG. 2. The angular dependence of the DDSCS for XNLC in the plane of the incoming wave vector and polarization [ $\omega_{\text{in}} = 18.37$  a.u. ( $\approx 500$  eV)]. The pattern is shown for  $\omega_q = 27.56$  a.u. ( $\approx 750$  eV) (red solid line) and  $\omega_q = 31.24$  a.u. ( $\approx 850$  eV) (red dashed line), where each data set represents the sum of two orthogonal polarizations of the scattered photon.

show no significant impact on the “full model” signal. These studies then lead us to conclude that indeed the dominant contributions to XNLC at  $\omega_{\text{in}} = 18.37$  a.u. ( $\approx 500$  eV) stem from the third-order terms depicted by the diagrams (29).

*Angular distribution of the scattered photon.* In addition to studying the fixed scattering geometry assumed in Ref. [25], we also employ our full model to investigate the angular distribution of nonlinearly scattered photons. To this end, we assume the same simulation parameters, but initially orient the scattered photon’s  $\mathbf{k}_q$  colinear to the wave vector of the incoming field  $\mathbf{k}_{\text{in}}$  (along the negative  $y$  axis). We then scan the DDSCS at two fixed  $\omega_q$  for various directions of  $\mathbf{k}_q$  in the  $y$ - $z$  plane, or respectively scattering angles from  $\vartheta = 0$  to  $\vartheta = \pi$ .

The resultant scattering patterns for  $\omega_q = 27.56$  a.u. ( $\approx 750$  eV) (red solid line) and  $\omega_q = 31.24$  a.u. ( $\approx 850$  eV) (red dashed line) are shown in Fig. 2, where  $\vartheta = 0$  denotes forward scattering,  $\vartheta = \pi$  backward scattering and  $\vartheta = \pi/2$  marks scattering along the polarization of the incoming field. Each data set represents the summed DDSCS for two orthogonal polarization states of the scattered photon.

In both cases, we can observe an angular distribution of the XNLC scattering probability that resembles a dipolar emission pattern for the scattered photon. They deviate, however, from this simple form in terms of a slight forward-backward asymmetry, favoring the forward direction. Moreover, there remains a nonvanishing probability for scattering to occur along the polarization direction of the incoming field (as pointed out previously in Ref. [18]).

## B. XNLC in helium at 4.0 keV

In this second application of our XNLC model, we extend our studies on helium into the regime of high photon energies. Choosing  $\omega_{\text{in}} = 147$  a.u. ( $\approx 4.0$  keV), we approach the conditions of Ref. [18]. Therein, Fuchs *et al.* present

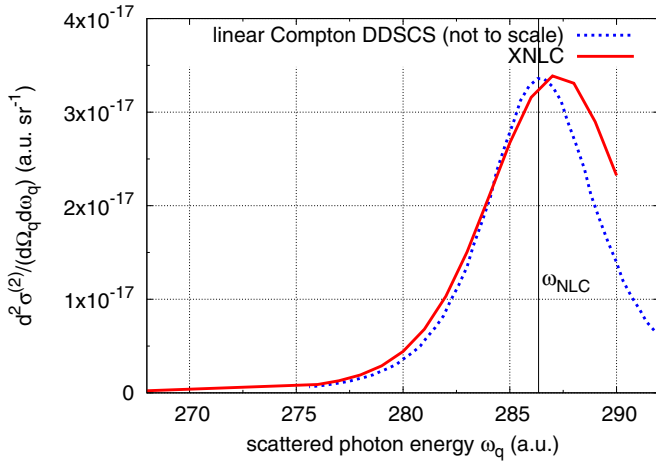


FIG. 3. The DDSCS for nonlinear Compton scattering at  $\omega_{in} = 147$  a.u. ( $\approx 4.0$  keV) in helium (red solid line) is contrasted with the linear Compton DDSCS at twice the incoming photon energy (blue dashed line, not to scale). The vertical line indicates the scattered photon energy expected from the free-electron model in both cases [cf. Eq. (1)].

evidence for a nonlinear scattering signal obtained from a solid beryllium target, which is irradiated with high intensity x-ray pulses at photon energies up to  $\omega_{in\_exp} = 358$  a.u. ( $\approx 9.7$  keV). This signal exhibits a significant redshift with respect to the nonlinear Compton line predicted by the free-electron model discussed in Sec. I. Accounting properly for the bound situation of the electrons during the XNLC process, we assess in the following study, whether we can observe a similar redshift and thus support the interpretation of the experimental findings in terms of (anomalous) XNLC.

We adjust the scattering geometry such that the incoming pulse [60] propagates along the negative  $y$  direction and bears a polarization parallel to the  $z$  axis. The scattered photon in the quantized mode ( $q$ ), on the other hand, is observed at a scattering angle of  $\vartheta = 0.75\pi$  ( $= 135^\circ$ ) in the  $y$ - $z$  plane, in accordance with Ref. [18]. Two orthogonal polarization states of the scattered photon are chosen for the propagation and their respective results added in the construction of the DDSCS. The result is plotted in Fig. 3 (red solid line). In contrast to the measured signal of Ref. [18], the resultant XNLC profile is peaked around the free-electron line expected from Eq. (1) ( $\omega_{NLC} \approx 286$  a.u.), showing no indication of an anomalous redshift.

Moreover, the profile exhibits a striking qualitative similarity to the linear Compton DDSCS for scattering at twice the incoming photon energy ( $\omega_{in\_linear} = 2\omega_{in} = 294$  a.u.), which we plot for comparison (blue dashed line). The latter result is obtained by means of the XATOM toolkit [61] and scaled to match the magnitude of the XNLC curve.

We want to point out that both observations can be confirmed in studies on beryllium (cf. Sec. III C) and strongly suggest in conjunction that our XNLC model does not support an anomalous Compton shift.

*XNLC mechanisms at higher photon energies.* Apart from our investigation into the anomalous redshift of XNLC, we may furthermore use the present results to once again study

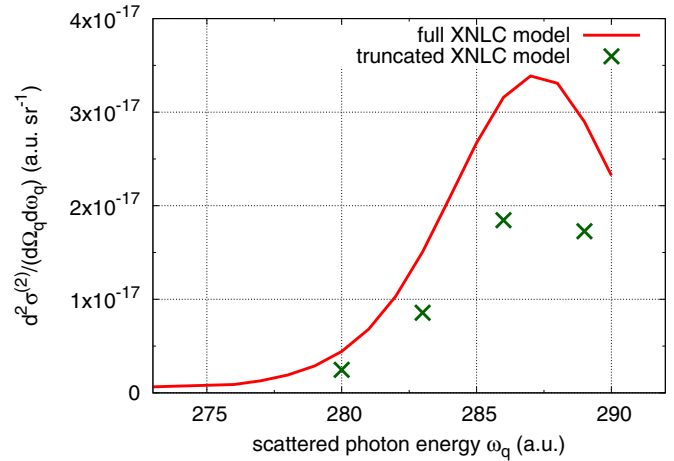


FIG. 4. Comparison of the DDSCS for nonlinear Compton scattering at  $\omega_{in} = 147$  a.u. ( $\approx 4.0$  keV) in helium obtained using the full XNLC model (red solid line) and the truncated model (green crosses).

the mechanisms underlying nonlinear scattering. Hereunto, we supplement the present results (cf. Fig. 3)—obtained using the full XNLC model—by an analysis in the truncated model as detailed in Sec. III A [cf. diagrams (32)]. The results of these restricted simulations are shown in Fig. 4 (green crosses) for a subset of the full model data points (red solid line). From the comparison, we can learn that the previously striking disparity of both descriptions (cf. Sec. III A) has decreased significantly at  $\omega_{in} = 147$  a.u. ( $\approx 4.0$  keV). In fact, rather than being dwarfed by the full model result, the truncated model now accounts for roughly half the DDSCS itself. Conversely, this nevertheless implies that the contributions omitted by Ref. [25] remain significant even at comparatively high photon energies.

### C. XNLC in beryllium at 9.7 keV

In the third application of our XNLC model, we directly address the experimental situation of Ref. [18] by simulating XNLC in atomic beryllium at  $\omega_{in} = 358$  a.u. ( $\approx 9.7$  keV). While this study promises the most immediate insight into the reported anomalous red shift, it also poses the biggest numerical challenge—by far. This is due to the fact that at such high photon energies scattering is largely caused by nondipole operators, which couple a broad range of angular momentum states. Treating these with sufficient numerical accuracy, unfortunately, exhausts our present computational capabilities, such that we could not reach converged results across the entire XNLC profile. Nevertheless, there is considerable insight to be gained from the partially converged DDSCS and its convergence behavior, as we report below.

Using the same scattering geometry as in Sec. III B, we perform XNLC simulations within different ranges of angular momentum states, in order to study the convergence behavior. The resultant DDSCSs are plotted in Fig. 5 (red symbols), labeled by the maximum angular momentum ( $l_{max}$ ) accounted for, respectively. For reference, note that the fastest of these calculations ( $l_{max} = 4$ ) can be performed in just under 8 h per

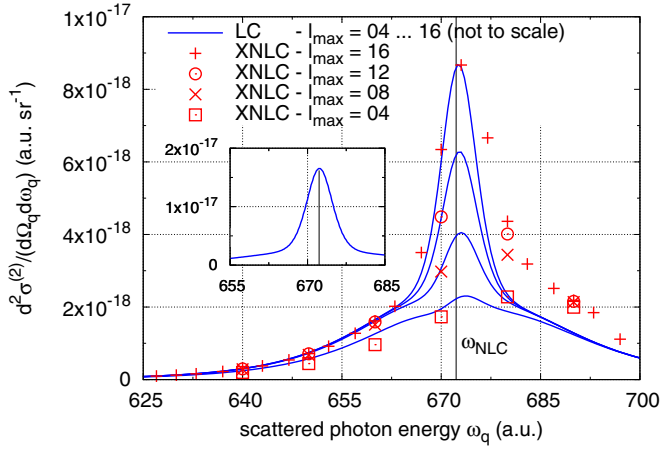


FIG. 5. DDSCSs for XNLC in beryllium at  $\omega_{in} = 358$  a.u. ( $\approx 9.7$  keV), sequences pertain to different stages of convergence with respect to  $l_{max}$  (red symbols). For the sake of readability, the lower- $l_{max}$  sequences are plotted at coarse intervals only. In addition, the DDSCSs for linear Compton scattering (LC) at  $\omega_{in,linear} = 2\omega_{in}$  is given (blue solid lines) in a sequence from small  $l_{max}$  (bottom) to large  $l_{max}$  (top). The scattering geometry for both sequences is fixed as in Sec. III B. The inlay shows the converged LC result employed as an extrapolation of the DDSCS for XNLC.

data point, while  $\sim 10$  days are required at  $l_{max} = 16$  using our current implementation and computational hardware [62].

We can clearly observe that the unconverged cross sections each attain their maximum value around the position predicted by the free-electron model [cf. Eq. (1),  $\omega_{NLC} \approx 672$  a.u.], without exhibiting an anomalous redshift. Moreover, we find from Fig. 5 that the wings of the XNLC profile are already well converged at  $l_{max} = 16$ , while only the magnitude of the peak still changes with  $l_{max}$ . This further disfavors the notion of an anomalous redshift, as it should have been visible predominantly in the region of the left-hand side wing. In conjunction with the previous results (Sec. III B), we therefore rule out the occurrence of an anomalous redshift of the the XNLC profile within our XNLC model.

In addition to the above discussion, we point out that the observed convergence behavior, i.e., converging from the wings inwards, mirrors a general trend. We have found the same behavior throughout our high-energy XNLC studies and—notably—also in the calculation of regular Compton profiles. Illustrating this point, we superimpose in Fig. 5 a sequence of DDSCSs (blue solid lines) that pertain to linear Compton scattering at twice the incoming photon energy [ $\omega_{in,linear} = 716$  a.u. ( $\approx 19.4$  keV)]. These results are calculated using the XATOM toolkit [61] by imposing the same  $l_{max}$  restrictions as in the corresponding XNLC cases. We stress that only a single overall scaling factor is required to match all linear Compton profiles remarkably well to the left-hand wings of their respective XNLC counterparts. This mutual agreement suggests the use of XATOM as a means of extrapolating the XNLC cross section towards numerically expensive regions. Doing so in the present case, we obtain an estimate of the converged cross section, which is shown as an inset in Fig. 5. Notably, angular momentum states up to  $l_{max} = 64$  have to be included in these calculations to reach

convergence. Attaining the same level of accuracy with our current XNLC implementation, however, would be highly impracticable—requiring an estimated computation time of  $\sim 2.6$  years per data point.

#### IV. CONCLUSION

In the present work, we have developed and implemented a theoretical approach to investigate x-ray scattering phenomena in atomic systems. The method is based on the explicit solution of the TDSE in terms of propagating a wave-function ansatz that accounts for both the atomic system and a quantized photonic mode. As the scheme is inherently nonperturbative, it allows us to treat x-ray scattering for a wide range of conditions. In particular, it is applicable to nonlinear cases as well as linear Compton scattering.

Making use of this versatility, we have benchmarked our approach on said process, reproducing the well-established linear Compton scattering cross sections.

After validation, we have first applied our method to a nonlinear scattering scenario at low photon energies [ $\omega_{in} = 18.37$  a.u. ( $\approx 500$  eV)], which has previously been investigated by Hopersky *et al.* [25]. For this setup, we have demonstrated within our model that the scattering cross section is unexpectedly dominated by contributions of  $\hat{\mathbf{p}} \cdot \hat{\mathbf{A}}$ -type operators, which would pertain to third-order terms in a perturbative analysis. This finding suggests that the original work [25] is insufficient to explain XNLC, as its calculations are *a priori* restricted to second order of perturbation theory.

In two subsequent studies, we have addressed XNLC at higher photon energies in an effort to trace the anomalous redshift reported by Fuchs *et al.* [18]. Hereunto, we have first evaluated the DDSCS for XNLC in helium at  $\omega_{in} = 147$  a.u. ( $\approx 4.0$  keV) before we have studied the experimental situation in atomic beryllium [ $\omega_{in,exp} = 358$  a.u. ( $\approx 9.7$  keV)]. In neither of these cases have we been able to observe anomalous Compton shifts. In fact, the resultant scattering profiles are consistently peaked around the expected value for the respective free-electron case and compare well to scaled cross sections of linear Compton scattering at twice the incoming photon energy. Notably, these findings are incompatible with the current interpretation of the nonlinear scattering signal in Ref. [18] in terms of XNLC. This allows for two possible conclusions—in our view—either of which resolves the conflict:

(1) Our modeling assumptions could be insufficient for the description of anomalous XNLC. This implies in particular that the anomaly is not (solely) caused by the presence of a binding atomic potential; or

(2) The interpretation of the experimental results in terms of a Compton-like nonlinear process could itself be invalid. This opens the discussion to consider alternative processes, like nonlinear parametric downconversion, as an explanation of the observed signal.

In our opinion, both routes warrant further investigation and immediately suggest certain steps to this effect. In the first case, the assumed failure of our present model consequentially provides indications as to the effects responsible. It would in particular suggest an increased importance of multielectron or solid-state effects, both of which are not yet



accounted for. Proceeding to include electronic correlation effects into our model can be achieved on the level of TDCIS by retrofitting DVR-based Coulomb operators, for instance, in the spirit of Ref. [63]. On the experimental side, studies of disordered (gaseous or liquid) targets can be employed to place constraints on speculative solid-state effects. In the second case, dedicated theoretical investigations are required in order to identify alternative nonlinear scattering processes. The essential test of the XNLC interpretation of Ref. [18], however, would be provided by a measurement setup that can detect XNLC photons and their accompanying recoil electrons simultaneously.

### ACKNOWLEDGMENTS

This work has been supported by the cluster of excellence ‘The Hamburg Centre for Ultrafast Imaging’ of the Deutsche Forschungsgemeinschaft (DFG) - EXC 1074 - project ID 194651731. D.A.R. was supported by the AMOS program within the Chemical Sciences Division of the Office of Basic Energy Sciences, Office of Science, U.S. Department of Energy and, during his stay at DESY in Hamburg, the Stephenson Distinguished Visitor Programme. The authors gratefully acknowledge computational support from the RRZ Hamburg. D.K. thanks M. Simmermacher, K. Mulack, and L. Inhester for prolific discussions.

### APPENDIX A: NUMERICAL IMPLEMENTATION

With the basic theory of our model outlined in Sec. II, we want to elaborate at this point more on its numerical implementation. We begin from the EOMs [Eqs. (17)–(20)], which in their present form do not yet lend themselves to immediate numerical solution. Instead, we first need to transform them into a more efficient representation (Appendix A 1) and moreover, impose appropriate limitations of the simulated space in terms of absorbing boundary conditions (Appendix A 2). Both measures, however, leave the above logic conceptually unchanged.

#### 1. Basis transformation

The EOMs in their current form [Eqs. (17)–(20)]—though conceptually simple—remain prohibitively expensive in their numerical solution. This is due to the partially inefficient choice of HFS orbitals as the single-particle basis. While the occupied orbitals  $|\varphi_i\rangle$  lend themselves naturally to the representation of “holes” in our expansion about the HFS ground state, their unoccupied counterparts  $|\varphi_a\rangle$  are an inefficient representation of the excited states. Their delocalized nature and the absence of selection rules—we do not impose the dipole approximation, for instance—lead to nonsparse coupling matrices  $\langle\varphi_c|\hat{\mathbf{A}}^2(\hat{\mathbf{r}}, t)|\varphi_a\rangle$  and  $\langle\varphi_c|\hat{\mathbf{p}}\cdot\hat{\mathbf{A}}(\hat{\mathbf{r}}, t)|\varphi_a\rangle$  on the right-hand side of Eqs. (18) and (20), which quickly exhaust computational resources. Notably, even the “smallest” numerical case presented in this article (Sec. III A) would require us to store multiple matrices of  $\approx 68$  gigabytes in size.

In order to alleviate this computational burden, while keeping the occupied orbitals in place, we resort to a partial basis transformation. We relate all unoccupied orbitals  $|\varphi_a\rangle$  to a new

set of basis functions  $|\rho_\alpha\rangle$ :

$$\rho_\alpha(\mathbf{r}) = \frac{g_{t_\alpha}(|\mathbf{r}|)}{|\mathbf{r}|} Y_{l_\alpha m_\alpha}(\Omega_{\mathbf{r}}) \quad (\text{A1})$$

via the unitary transformation

$$|\varphi_p\rangle = \sum_{\alpha} U_{\alpha p} |\rho_\alpha\rangle. \quad (\text{A2})$$

In contrast to Eq. (13), the new basis functions feature strongly localized radial components  $g_{t_\alpha}(|\mathbf{r}|)$ , which form a DVR [64,65] in the  $|\mathbf{r}|$  domain. Thereby, the radial part of any local operator—including  $\hat{\mathbf{A}}$  and  $\hat{\mathbf{A}}^2$ —is rendered (approximately) diagonal, which already yields a considerable reduction of the respective matrices’ sizes. For the resultant operators, we can then afford on-the-fly generation on modern GPU accelerators and thus bypass memory bottlenecks altogether. The initial construction of *nonlocal* operators as well as the preparation of the DVR functions themselves proceeds via the intermediate use of a finite-elements method (FEM) (cf. Ref. [66]). Notably, we adhere to the convention of quoted work to choose *all* radial functions real, which implies for the transformation coefficients

$$U_{\alpha p} = \langle g_{t_\alpha} | u_{n_p l_p} \rangle \delta_{l_\alpha l_p} \delta_{m_\alpha m_p} = U_{\alpha p}^*. \quad (\text{A3})$$

Applying the transformation [Eq. (A2)] to the EOM—starting from Eqs. (17) and (19)—we rewrite unoccupied orbitals in expressions such as, e.g.,

$$\sum_{i,a} \alpha_i^a(t) \langle \varphi_i | \hat{H}_{\text{any}} | \varphi_a \rangle = \sum_{i,\alpha} \sum_a U_{\alpha a} \alpha_i^a(t) \langle \varphi_i | \hat{H}_{\text{any}} | \rho_\alpha \rangle. \quad (\text{A4})$$

At this point, the old expansion coefficients  $\alpha_i^a(t)$  and  $\beta_j^b(t)$  become cumbersome, as they no longer reference the excited states in use. We therefore contract them with the introduced transformation matrices, defining new, adapted expansion coefficients as

$$\mathcal{A}_i^\alpha(t) = \sum_a U_{\alpha a} \alpha_i^a(t) \quad (\text{A5})$$

and analogously  $\mathcal{B}_j^\beta(t)$  for  $\beta_j^b(t)$ . With the above in place, Eqs. (17) and (19) read

$$i \frac{\partial}{\partial t} \alpha_0 = 2 \alpha_0 \langle \hat{H}_{00} \rangle_{\text{occ}} + \sqrt{2} \sum_{i,\alpha} \mathcal{A}_i^\alpha \langle \varphi_i | \hat{H}_{00} | \rho_\alpha \rangle + 2 \beta_0 \langle \hat{H}_{\downarrow} \rangle_{\text{occ}} + \sqrt{2} \sum_{j,\beta} \mathcal{B}_j^\beta \langle \varphi_j | \hat{H}_{\downarrow} | \rho_\beta \rangle, \quad (\text{A6})$$

$$i \frac{\partial}{\partial t} \beta_0 = 2 \alpha_0 \langle \hat{H}_{\uparrow} \rangle_{\text{occ}} + \sqrt{2} \sum_{i,\alpha} \mathcal{A}_i^\alpha \langle \varphi_i | \hat{H}_{\uparrow} | \rho_\alpha \rangle + 2 \beta_0 \langle \hat{H}_{11} \rangle_{\text{occ}} + \sqrt{2} \sum_{j,\beta} \mathcal{B}_j^\beta \langle \varphi_j | \hat{H}_{11} | \rho_\beta \rangle. \quad (\text{A7})$$

We proceed similarly for the EOM of  $\alpha_k^c(t)$  and  $\beta_k^c(t)$  [Eqs. (18) and (20)], replacing the ket states  $|\varphi_a\rangle$  and  $|\varphi_b\rangle$  as previously shown alongside redefining their coefficients. In addition, we have to transform the occurring bra states  $\langle\varphi_c|$ ,

as well as the expansion coefficients  $\alpha_{\text{any}}^c$  and  $\beta_{\text{any}}^c$  themselves. To this end, we subject the two sets of EOM to an additional overall transformation of the form

$$\sum_c U_{\gamma c} \left( i \frac{\partial}{\partial t} \alpha_k^c(t) \right) = i \frac{\partial}{\partial t} \mathcal{A}_k^\gamma(t) \quad (\text{A8})$$

and again analogous for  $\beta_k^c(t)$ .

While this procedure yields the desired expansion coefficients, it fails to transform the states  $\langle \varphi_c |$  due to the incomplete sum over  $c$  (only virtual orbitals are included; cf. Sec. II B). This problem, in turn, is resolved by augmenting the summation to include occupied orbitals (here labeled by the index  $l$ ) as well:

$$\begin{aligned} \sum_c U_{\gamma c} \langle \varphi_c | &= \sum_p^{\text{all}} U_{\gamma p} \langle \varphi_p | - \sum_l U_{\gamma l} \langle \varphi_l | \\ &= \langle \rho_\gamma | - \sum_l U_{\gamma l} \langle \varphi_l |, \end{aligned} \quad (\text{A9})$$

$$\begin{aligned} i \frac{\partial}{\partial t} \mathcal{A}_k^\gamma &= 2 \mathcal{A}_k^\gamma \langle \hat{H}_{00} \rangle_{\text{occ}} + \sqrt{2} \alpha_0 \langle \rho_\gamma | \hat{H}_{00} | \varphi_k \rangle - \sum_i \mathcal{A}_i^\gamma \langle \varphi_i | \hat{H}_{00} | \varphi_k \rangle + \sum_\alpha \mathcal{A}_k^\alpha \langle \rho_\gamma | \hat{H}_{00} | \rho_\alpha \rangle \\ &\quad - \sum_l U_{\gamma l} \left( \sqrt{2} \alpha_0 \langle \varphi_l | \hat{H}_{00} | \varphi_k \rangle + \sum_\alpha \mathcal{A}_k^\alpha \langle \varphi_l | \hat{H}_{00} | \rho_\alpha \rangle \right) + 2 \mathcal{B}_k^\gamma \langle \hat{H} \downarrow \rangle_{\text{occ}} + \sqrt{2} \beta_0 \langle \rho_\gamma | \hat{H} \downarrow | \varphi_k \rangle \\ &\quad - \sum_j \mathcal{B}_j^\gamma \langle \varphi_j | \hat{H} \downarrow | \varphi_k \rangle + \sum_\beta \mathcal{B}_k^\beta \langle \rho_\gamma | \hat{H} \downarrow | \rho_\beta \rangle - \sum_l U_{\gamma l} \left( \sqrt{2} \beta_0 \langle \varphi_l | \hat{H} \downarrow | \varphi_k \rangle + \sum_\beta \mathcal{B}_k^\beta \langle \varphi_l | \hat{H} \downarrow | \rho_\beta \rangle \right), \quad (\text{A11}) \\ i \frac{\partial}{\partial t} \mathcal{B}_k^\gamma &= 2 \mathcal{A}_k^\gamma \langle \hat{H} \uparrow \rangle_{\text{occ}} + \sqrt{2} \alpha_0 \langle \rho_\gamma | \hat{H} \uparrow | \varphi_k \rangle - \sum_i \mathcal{A}_i^\gamma \langle \varphi_i | \hat{H} \uparrow | \varphi_k \rangle + \sum_\alpha \mathcal{A}_k^\alpha \langle \rho_\gamma | \hat{H} \uparrow | \rho_\alpha \rangle \\ &\quad - \sum_l U_{\gamma l} \left( \sqrt{2} \alpha_0 \langle \varphi_l | \hat{H} \uparrow | \varphi_k \rangle + \sum_\alpha \mathcal{A}_k^\alpha \langle \varphi_l | \hat{H} \uparrow | \rho_\alpha \rangle \right) + 2 \mathcal{B}_k^\gamma \langle \hat{H}_{11} \rangle_{\text{occ}} + \sqrt{2} \beta_0 \langle \rho_\gamma | \hat{H}_{11} | \varphi_k \rangle \\ &\quad - \sum_j \mathcal{B}_j^\gamma \langle \varphi_j | \hat{H}_{11} | \varphi_k \rangle + \sum_\beta \mathcal{B}_k^\beta \langle \rho_\gamma | \hat{H}_{11} | \rho_\beta \rangle - \sum_l U_{\gamma l} \left( \sqrt{2} \beta_0 \langle \varphi_l | \hat{H}_{11} | \varphi_k \rangle + \sum_\beta \mathcal{B}_k^\beta \langle \varphi_l | \hat{H}_{11} | \rho_\beta \rangle \right), \quad (\text{A12}) \end{aligned}$$

which—in conjunction with Eqs. (A6) and (A7)—serve as the basis of our XNLC implementation.

As a concluding remark, we want to point out that our partial transformation of the CIS-like equations resembles the more abstract approach of Rohringer *et al.* in Ref. [67].

## 2. Complex absorbing potential

This section is concerned with the numerical intricacies arising at the boundary of the spatial simulation range. Once an outgoing electron encounters this boundary, it undergoes reflection as off an open ending of a waveguide. Given that such reflections would contaminate any further time evolution and thereby distort the results in an unphysical manner, preventive measures have to be taken.

A straightforward remedy is to increase the size of the simulation box up to the point at which it encloses all electronic dynamics for the duration of the simulation (for an example consider Ref. [68]). However, in view of the potentially huge

albeit at the cost of introducing an additional projector. This reflects the fact that the radially localized functions  $|\rho_\gamma\rangle$  are not intrinsically orthogonal to the occupied orbitals  $|\varphi_l\rangle$ . Implemented into the EOM, the projector prevents artificial overlap of excited states with the ground state by ensuring reorthogonalization at each time step.

A closely related issue concerns the expansion coefficients, which should respect the orthogonality of occupied and virtual orbitals ( $\langle \varphi_i | \varphi_a \rangle = \delta_{ia} = 0$ ) at all times, implying the identity

$$\begin{aligned} \sum_\alpha \mathcal{A}_i^\alpha(t) U_{\alpha k}^* &= \sum_\alpha \left( \sum_a \alpha_i^a(t) U_{\alpha a} \right) U_{\alpha k}^* \\ &= \sum_a \alpha_i^a(t) \delta_{ak} = 0. \end{aligned} \quad (\text{A10})$$

An analogous expression holds for  $\mathcal{B}_j^\beta(t)$ .

Bearing this in mind and applying the former, Eqs. (18) and (20) become

boxes required and the associated computational cost, we refrain from such a solution.

Alternatively, the boundary region may be modified to absorb outgoing electronic flux rather than reflect it. Hereunto, we adopt the widely used method of applying a complex absorbing potential (CAP) [69–74]. This scheme involves the addition of a weak complex potential to the Hamiltonian, which induces the wave function to decay in the outer region of the simulation volume. While CAPs are themselves not completely devoid of artefacts, their behavior has been thoroughly studied and well understood [75–77].

We implement the CAP as the additional complex one-body potential:

$$V_{\text{CAP}}(|\hat{\mathbf{r}}\rangle) = -i\eta W(|\hat{\mathbf{r}}\rangle) = -i\eta(|\hat{\mathbf{r}}\rangle - r_{\text{abs}})^2 \Theta(|\hat{\mathbf{r}}\rangle - r_{\text{abs}}), \quad (\text{A13})$$

sporting a purely radial dependence. The input parameters  $\eta \in \mathbb{R}^+$  and  $r_{\text{abs}} \in \mathbb{R}^+$  are employed to specify the strength

and the onset radius of the absorbing region, respectively, with  $\Theta(|\hat{\mathbf{r}}| - r_{\text{abs}})$  denoting the Heaviside step function. During the propagation of the EOM, the CAP term is added directly to the HFS potential acting on the excited states, while in accordance with Ref. [26] the ground state (i.e., any occupied orbital) is assumed to be unaffected.

While this procedure stabilizes the numerical propagation in the desired manner, it also inevitably alters the norm of the propagated wave function. This artifact, however, can be used to our advantage, as the absorbed part of the wave function corresponds to the outgoing (electronic) flux, which—in turn—relates to the scattering probability  $P_q$  (cf. Sec. IID).

In order to obtain the absorbed portion, we adapt a scheme presented in Ref. [26]. Hereunto, we focus on the reduced density matrix (RDM) of the photonic two-level system:

$$\hat{\rho}^{\text{phot}}(t) = \text{Tr}_{\text{el}}(\hat{\rho}(t)) = \text{Tr}_{\text{el}}(|\Psi(t)\rangle\langle\Psi(t)|), \quad (\text{A14})$$

writing  $\text{Tr}_{\text{el}}(\dots)$  to signify the trace over all electronic states. The temporal evolution of the photonic RDM is governed by

$$\frac{\partial}{\partial t} \hat{\rho}^{\text{phot}}(t) = -i \text{Tr}_{\text{el}}([\hat{H}, \hat{\rho}(t)]) - 2\eta \text{Tr}_{\text{el}}(\hat{W} \hat{\rho}(t)), \quad (\text{A15})$$

where  $\hat{H}$  denotes the CAP-free Hamiltonian and  $\hat{W}$ —reflecting the influence of the CAP—is understood to be  $\hat{W} = \sum_n W(|\hat{\mathbf{r}}_n|)$ . Following Ref. [26], we account for the discrepancy of physical and artificial evolution in terms of a correction term:

$$\delta \hat{\rho}^{\text{phot}}(t) = \hat{\rho}_{\text{PHYS}}^{\text{phot}}(t) - \hat{\rho}^{\text{phot}}(t), \quad (\text{A16})$$

which is generated solely from the CAP absorption:

$$\frac{\partial}{\partial t} \delta \hat{\rho}^{\text{phot}}(t) = 2\eta \text{Tr}_{\text{el}}(\hat{W} \hat{\rho}(t)). \quad (\text{A17})$$

Focusing on the 11 term of the photonic RDM, i.e., the absorbed flux in the one-photon sector, we write

$$\frac{\partial}{\partial t} \delta \rho_{11}^{\text{phot}}(t) = 2\eta \sum_{i,\alpha} W(r_\alpha) |\mathcal{B}_i^\alpha(t)|^2. \quad (\text{A18})$$

The above expression may now be integrated numerically alongside the propagation of the expansion coefficients and thereby yield the desired  $P_q$  [78].

## APPENDIX B: VALIDATION

Before investigating XNLC, we have sought to validate the functioning of our (numerical) model. Hereunto, we have made use of its versatility and applied it to several, well-studied phenomena for benchmarking. Conducting, for instance, photoabsorption simulations, we have successfully tested the conventional aspects of our wave-packet propagation scheme. At this point, however, we shall focus our discussion on the model's unique feature—the quantized mode (q)—and assess its implementation. To this end, the investigation of regular Compton scattering has provided a natural test bed, requiring essentially the same mechanisms as XNLC.

In the following sections, we briefly outline the framework of these tests (Appendix B 1) and show results for two selected cases at (mean) incoming photon energies of  $\omega_{\text{in}} = 18.37$  a.u. ( $\approx 500$  eV) in Appendix B 2 and  $\omega_{\text{in}} = 294$  a.u. ( $\approx 8.0$  keV) in Appendix B 3.

## 1. Testing framework

Analogous to the nonlinear case, we can evaluate the linear scattering results in terms of a DDSCS as given by Eq. (26). This time, though, we assume the scattering probability  $P_q$  to depend linearly on the incoming field and thus normalize Eq. (26) by the linear fluence  $F_{\text{in}}^{(1)}$ :

$$F_{\text{in}}^{(1)} = \int_0^{t_{\text{end}}} dt J_{\text{in}}(t) = \int_0^{t_{\text{end}}} dt \frac{\alpha \omega_{\text{in}}}{2\pi} [A(t)]^2, \quad (\text{B1})$$

instead of  $F_{\text{in}}^{(2)}$ . As a benchmark to the DDSCS obtained in this way, we employ Compton spectra generated by the XATOM toolkit [61,79]. It should be noted that these spectra reflect the popular  $\hat{\mathbf{A}}^2$  approximation (cf., e.g., Ref. [21]), i.e., scattering is described exclusively in terms of the  $\hat{\mathbf{A}}^2$  diagram from first order of perturbation theory:



$$(\text{B2})$$

In contrast, our model generally allows for scattering into the quantized mode (q) via multiple terms of the Hamiltonian [cf. Eq. (23)]:



$$(\text{B3})$$

in a nonperturbative manner. While some of these additional terms can have noticeable effects at low photon energies (see indication in Appendix B 2) or in resonant scattering processes (cf., e.g., Ref. [80]), they generally become insignificant at high photon energies and beyond resonances, justifying the XATOM benchmark.

## 2. Compton scattering at 500 eV

Employing the same scattering setup as in Sec. III A, but with  $\omega_q$ —the photon energy of the quantized mode (q)—tuned below  $\omega_{\text{in}} = 18.37$  a.u. ( $\approx 500$  eV), we investigate regular Compton scattering in helium at comparatively low photon energies. We sample  $\omega_q$  from 11 to 17 a.u. in coarse steps of 1 a.u. and plot the resultant DDSCS in Fig. 6. There, we give results both for our full XNLC model [red crosses (+)] and a truncated version [green crosses (x)]—corresponding to the  $\hat{\mathbf{A}}^2$  approximation—on top of the XATOM reference (blue solid line) [81]. Note that we trace only the inelastic portion of the scattering process that involves the ionization of the atomic system. This fact is indicated in Fig. 6 by the spectral gap towards the position of the elastic line (18.37 a.u.), measuring the ionization potential (IP).

We find excellent agreement of the truncated model with the reference data, which validates the basic functionality of our implementation. In addition—by choosing a logarithmic scale—we can expose the slight deviation of the full model from its truncated counterpart. This observation, in turn, is in good agreement with recent findings by Drukarev *et al.* [82]. In quoted work, its authors demonstrate perturbatively that scattering contributions from  $\hat{\mathbf{p}} \cdot \hat{\mathbf{A}}$  terms gain in importance with respect to  $\hat{\mathbf{A}}^2$  contributions on going towards lower scattered photon energies.

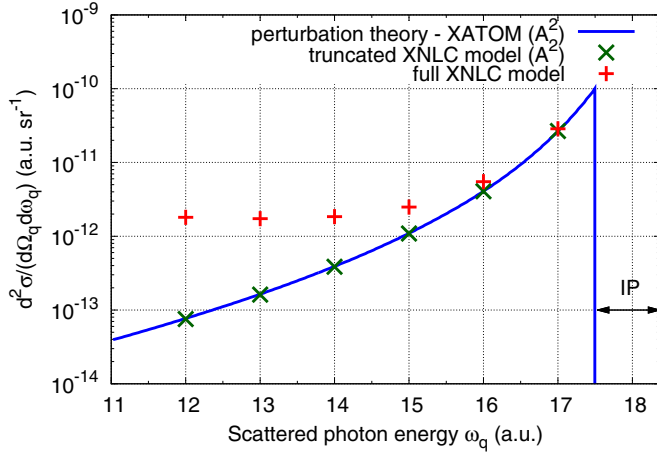


FIG. 6. The DDSCS for regular Compton scattering in helium calculated with the full XNLC model [red crosses (+)] as well as using the  $\hat{A}^2$  approximation [green crosses ( $\times$ )] and the XATOM toolkit (blue solid line). Here, the polarization of incoming and scattered photons is chosen parallel and the scattering occurs at an angle of  $\vartheta = \pi/2$  in the plane perpendicular to the polarization vector. The incoming photons are of mean energy  $\omega_{\text{in}} = 18.37$  a.u. ( $\approx 500$  eV).

We want to emphasize that these results rely crucially on the capability of our implementation to account for light-matter coupling beyond the dipole approximation [83]. Without this functionality, any inelastic scattering due to  $\hat{A}^2$  contributions, for instance, would be forbidden.

### 3. Compton scattering at 8.0 keV

As an example at higher photon energies, we present our valdatory studies of regular Compton scattering in helium at  $\omega_{\text{in}} = 294$  a.u. ( $\approx 8.0$  keV). Here, we choose the same scattering geometry as in our XNLC simulations of Sec. III B. By

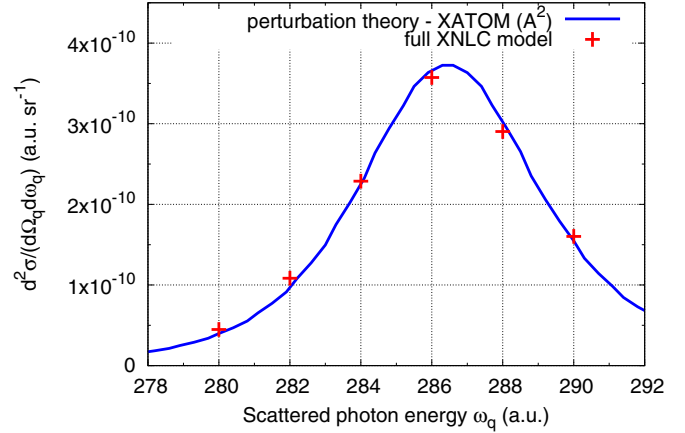


FIG. 7. The DDSCS for regular Compton scattering in helium calculated with the full XNLC model [red crosses (+)] and the XATOM toolkit (blue solid line). The mean incoming photon energy is chosen to be  $\omega_{\text{in}} = 294$  a.u. ( $\approx 8.0$  keV) and the scattering geometry is fixed as in Sec. III B.

employing twice the incoming photon energy, while focusing only on the linear scattering process, we also achieve the same kinematics as in Sec. III B's study and ultimately probe similarly extensive coupling matrices. We plot the results of our time-dependent scattering simulations in Fig. 7. There, DDSCS values as obtained from our full XNLC model [red crosses (+)] are given for a range of scattered photon energies (280–290 a.u.). In addition, we show the XATOM reference (blue solid line). Once again, we observe very good agreement of both approaches, verifying the functioning of our XNLC model.

Note that we abstain from plotting separate results of the truncated XNLC model in contrast to the previous Fig. 6 (Appendix B 2). In the present case, such data points are redundant, as they coincide with the results of the full model.

- 
- [1] W. Ackermann, G. Asova, V. Ayvazyan, A. Azima, N. Baboi, J. Bahr, V. Balandin, B. Beutner, A. Brandt, A. Bolzmann *et al.*, Operation of a free-electron laser from the extreme ultraviolet to the water window, *Nat. Photon.* **1**, 336 (2007).
- [2] <https://flash.desy.de/>.
- [3] P. Emma, R. Akre, J. Arthur, R. Bionta, C. Bostedt, J. Bozek, A. Brachmann, P. Bucksbaum, R. Coffee, F.-J. Decker *et al.*, First lasing and operation of an angstrom-wavelength free-electron laser, *Nat. Photon.* **4**, 641 (2010).
- [4] <https://lcls.slac.stanford.edu/>.
- [5] T. Ishikawa, H. Aoyagi, T. Asaka, Y. Asano, N. Azumi, T. Bizen, H. Ego, K. Fukami, T. Fukui, Y. Furukawa *et al.*, A compact x-ray free-electron laser emitting in the sub-angstrom region, *Nat. Photon.* **6**, 540 (2012).
- [6] <http://xfel.riken.jp/eng/>.
- [7] R. Neutze, R. Wouts, D. van der Spoel, E. Weckert, and J. Hajdu, Potential for biomolecular imaging with femtosecond x-ray pulses, *Nature (London)* **406**, 752 (2000).
- [8] L. Young, E. P. Kanter, B. Krässig, Y. Li, A. M. March, S. T. Pratt, R. Santra, S. H. Southworth, N. Rohringer, L. F. DiMauro *et al.*, Femtosecond electronic response of atoms to ultra-intense x-rays, *Nature (London)* **466**, 56 (2010).
- [9] M. Hoener, L. Fang, O. Kornilov, O. Gessner, S. T. Pratt, M. Gühr, E. P. Kanter, C. Blaga, C. Bostedt, J. D. Bozek *et al.*, Ultraintense X-Ray Induced Ionization, Dissociation, and Frustrated Absorption in Molecular Nitrogen, *Phys. Rev. Lett.* **104**, 253002 (2010).
- [10] L. Fang, M. Hoener, O. Gessner, F. Tarantelli, S. T. Pratt, O. Kornilov, C. Buth, M. Gühr, E. P. Kanter, C. Bostedt *et al.*, Double Core-Hole Production in  $n_2$ : Beating the Auger Clock, *Phys. Rev. Lett.* **105**, 083005 (2010).
- [11] G. Doumy, C. Roedig, S.-K. Son, C. I. Blaga, A. D. DiChiara, R. Santra, N. Berrah, C. Bostedt, J. D. Bozek, P. H. Bucksbaum *et al.*, Nonlinear Atomic Response to Intense Ultrashort X-Rays, *Phys. Rev. Lett.* **106**, 083002 (2011).
- [12] E. P. Kanter, B. Krässig, Y. Li, A. M. March, P. Ho, N. Rohringer, R. Santra, S. H. Southworth, L. F. DiMauro, G. Doumy *et al.*, Unveiling and Driving Hidden Resonances with High-Fluence, High-Intensity X-Ray Pulses, *Phys. Rev. Lett.* **107**, 233001 (2011).

- [13] T. E. Glover, D. M. Fritz, M. Cammarata, T. K. Allison, S. Coh, J. M. Feldkamp, H. Lemke, D. Zhu, Y. Feng, R. N. Coffee, M. Fuchs, S. Ghimire, J. Chen, S. Shwartz, D. A. Reis, S. E. Harris, and J. B. Hastings, X-ray and optical wave mixing, *Nature (London)* **488**, 603 (2012).
- [14] K. Tamasaku, M. Nagasono, H. Iwayama, E. Shigemasa, Y. Inubushi, T. Tanaka, K. Tono, T. Togashi, T. Sato, T. Katayama *et al.*, Double Core-Hole Creation by Sequential Attosecond Photoionization, *Phys. Rev. Lett.* **111**, 043001 (2013).
- [15] C. Weninger, M. Purvis, D. Ryan, R. A. London, J. D. Bozek, C. Bostedt, A. Graf, G. Brown, J. J. Rocca, and N. Rohringer, Stimulated Electronic X-Ray Raman Scattering, *Phys. Rev. Lett.* **111**, 233902 (2013).
- [16] K. Tamasaku, E. Shigemasa, Y. Inubushi, T. Katayama, K. Sawada, H. Yumoto, H. Ohashi, H. Mimura, M. Yabashi, K. Yamauchi *et al.*, X-ray two-photon absorption competing against single and sequential multiphoton processes, *Nat. Photon.* **8**, 313 (2014).
- [17] S. Shwartz, M. Fuchs, J. B. Hastings, Y. Inubushi, T. Ishikawa, T. Katayama, D. A. Reis, T. Sato, K. Tono, M. Yabashi *et al.*, X-Ray Second Harmonic Generation, *Phys. Rev. Lett.* **112**, 163901 (2014).
- [18] M. Fuchs, M. Trigo, J. Chen, S. Ghimire, S. Shwartz, M. Kozina, M. Jiang, T. Henighan, C. Bray, G. Ndabashimiye *et al.*, Anomalous nonlinear x-ray Compton scattering, *Nat. Phys.* **11**, 964 (2015).
- [19] L. S. Brown and T. W. B. Kibble, Interaction of intense laser beams with electrons, *Phys. Rev.* **133**, A705 (1964).
- [20] A. H. Compton, A quantum theory of the scattering of x-rays by light elements, *Phys. Rev.* **21**, 483 (1923).
- [21] R. H. Pratt, L. A. LaJohn, V. Florescu, T. Surić, B. K. Chatterjee, and S. C. Roy, Compton scattering revisited, *Radiat. Phys. Chem.* **79**, 124 (2010).
- [22] Note that the relation (1) is simplified with respect to the original publication [19] omitting an intensity-dependent shift, which is negligible in the present case.
- [23] Note that employing atomic units (a.u.), we set  $\hbar = m_e = |e| = 1$  and  $c = 1/\alpha$  throughout the present article. Herein,  $\hbar$  is the reduced Planck constant,  $m_e$  is the mass of an electron, and  $e$  is its charge. Furthermore,  $c$  denotes the speed of light in vacuo and  $\alpha$  marks the fine-structure constant.
- [24] M. Dondera and H. Bachau, Exploring above-threshold ionization of hydrogen in an intense x-ray laser field through nonperturbative calculations, *Phys. Rev. A* **85**, 013423 (2012).
- [25] A. N. Hoppersky, A. M. Nadolinsky, and S. A. Novikov, Compton scattering of two x-ray photons by an atom, *Phys. Rev. A* **92**, 052709 (2015).
- [26] L. Greenman, P. J. Ho, S. Pabst, E. Kamarchik, D. A. Mazziotti, and R. Santra, Implementation of the time-dependent configuration-interaction singles method for atomic strong-field processes, *Phys. Rev. A* **82**, 023406 (2010).
- [27] S. Pabst, L. Greenman, P. J. Ho, D. A. Mazziotti, and R. Santra, Decoherence in Attosecond Photoionization, *Phys. Rev. Lett.* **106**, 053003 (2011).
- [28] S. Pabst, A. Sytcheva, A. Moulet, A. Wirth, E. Goulielmakis, and R. Santra, Theory of attosecond transient-absorption spectroscopy of krypton for overlapping pump and probe pulses, *Phys. Rev. A* **86**, 063411 (2012).
- [29] D. Krebs, S. Pabst, and R. Santra, Introducing many-body physics using atomic spectroscopy, *Am. J. Phys.* **82**, 113 (2014).
- [30] A. Karamatskou, Nonlinear effects in photoionization over a broad photon-energy range within the tdcis scheme, *J. Phys. B* **50**, 013002 (2017).
- [31] A. Karamatskou and R. Santra, Time-dependent configuration-interaction-singles calculation of the 5p-subshell two-photon ionization cross section in xenon, *Phys. Rev. A* **95**, 013415 (2017).
- [32] R. E. Wagner, Q. Su, and R. Grobe, Time-resolved Compton scattering for a model fermion-boson system, *Phys. Rev. A* **82**, 022719 (2010).
- [33] R. E. Wagner, M. R. Ware, Q. Su, and R. Grobe, Space-time properties of a boson-dressed fermion for the Yukawa model, *Phys. Rev. A* **82**, 032108 (2010).
- [34] R. E. Wagner, M. R. Ware, B. T. Shields, Q. Su, and R. Grobe, Space-Time Resolved Approach for Interacting Quantum Field Theories, *Phys. Rev. Lett.* **106**, 023601 (2011).
- [35] I. A. Gonoskov, N. Tsatrafyllis, I. K. Kominis, and P. Tzallas, Quantum optical signatures in strong-field laser physics: Infrared photon counting in high-order-harmonic generation, *Sci. Rep.* **6**, 32821 (2016).
- [36] M. Ruggenthaler, J. Flick, C. Pellegrini, H. Appel, I. V. Tokatly, and A. Rubio, Quantum-electrodynamical density-functional theory: Bridging quantum optics and electronic-structure theory, *Phys. Rev. A* **90**, 012508 (2014).
- [37] J. Flick, M. Ruggenthaler, H. Appel, and A. Rubio, Kohn-Sham approach to quantum electrodynamic density-functional theory: Exact time-dependent effective potentials in real space, *Proc. Natl. Acad. Sci. USA* **112**, 15285 (2015).
- [38] J. Flick, M. Ruggenthaler, H. Appel, and A. Rubio, Atoms and molecules in cavities, from weak to strong coupling in quantum-electrodynamics (qed) chemistry, *Proc. Natl. Acad. Sci. USA* **114**, 3026 (2017).
- [39] C. A. Navarro, N. Hitschfeld-Kahler, and L. Mateu, A survey on parallel computing and its applications in data-parallel problems using GPU architectures, *Commun. Comput. Phys.* **15**, 285 (2014).
- [40] Note for the case of  $\omega_{in} = 4$  keV, for instance, that the small ratios of  $\frac{\hbar\omega_{in}}{2m_e c^2} \approx 4 \times 10^{-3}$  and  $\frac{eA}{2m_e c^2} \lesssim 1 \times 10^{-3}$  suppress relativistic effects like pair production, while a maximally achievable Lorentz factor  $\gamma = 1.016$  justifies nonrelativistic kinematics.
- [41] R. Loudon, *The Quantum Theory of Light* (Oxford University Press, New York, 1983).
- [42] D. P. Craig and T. Thirunamachandran, *Molecular Quantum Electrodynamics* (Dover, New York, 1998).
- [43] J. C. Slater, A simplification of the Hartree-Fock method, *Phys. Rev.* **81**, 385 (1951).
- [44] J. C. Slater, Atomic radii in crystals, *J. Chem. Phys.* **41**, 3199 (1964).
- [45] H. P. Hanson, F. Herman, J. E. Lea, and S. Skillman, Hfs atomic scattering factors, *Acta Crystallogr.* **17**, 1040 (1964).
- [46] A. Rosen, D. E. Ellis, H. Adachi, and F. W. Averill, Calculations of molecular ionization energies using a self-consistent-charge Hartree-Fock-Slater method, *J. Chem. Phys.* **65**, 3629 (1976).
- [47] S.-K. Son and R. Santra, Monte Carlo calculation of ion, electron, and photon spectra of xenon atoms in x-ray free-electron laser pulses, *Phys. Rev. A* **85**, 063415 (2012).
- [48] E. L. Saldin, E. A. Schneidmiller, and M. V. Yurkov, *The Physics of Free Electron Lasers* (Springer-Verlag, Berlin, 2000).

- [49] Note that further possible shortcomings may be associated with the (artificial) mode segmentation of the XNLC analysis. In particular, this setup does not account for the (potential) interference of multiple modes, both in intermediate and final states. It in fact also entails the peculiarity that the simulated photon does not propagate spatially, as a single excitation of a single mode may not exhibit the behavior of a traveling wave packet. However—as suggested above—these deficiencies are likewise present in common perturbative scattering calculations, where they are not found to adversely affect the outcome. Therefore, we assume these limitations to be of minor significance in the present case, as well.
- [50] R. Santra, Concepts in x-ray physics, *J. Phys. B* **42**, 023001 (2009).
- [51] S. Pabst, L. Greenman, D. A. Mazziotti, and R. Santra, Impact of multichannel and multipole effects on the cooper minimum in the high-order-harmonic spectrum of argon, *Phys. Rev. A* **85**, 023411 (2012).
- [52] Note that we focus on closed-shell systems in the present work, for which the reference state  $|\Phi_0\rangle$  is a spin-singlet determinant. For these systems, all further relevant states within our model are likewise singlets, as the *spin-independent* Hamiltonian can only mediate transitions from  $|\Phi_0\rangle$  into other singlet states. Accordingly, the excited states' notation  $|\Phi_i^a\rangle$  implies the spin-symmetrized structure  $|\Phi_i^a\rangle = \frac{1}{\sqrt{2}}(\hat{c}_{a\uparrow}^\dagger \hat{c}_{i\uparrow} + \hat{c}_{a\downarrow}^\dagger \hat{c}_{i\downarrow})|\Phi_0\rangle$ , where the operators  $\hat{c}_{a\uparrow}^\dagger$  (or  $\hat{c}_{a\downarrow}^\dagger$ ) refer to the creation of an electron in an orbital  $|\varphi_a\rangle$  with the spin state  $\uparrow$  (or  $\downarrow$ ), while  $\hat{c}_{i\uparrow}$  (or  $\hat{c}_{i\downarrow}$ ) function analogously for an electron's annihilation.
- [53] Note that we drop any scalar contributions  $[C(t)]$  to the Hamiltonian that affect all states uniformly, as they may always be absorbed by a global gauge transformation  $|\Psi(t)\rangle \rightarrow e^{i \int_0^t d\tau C(\tau)} |\Psi(t)\rangle$ .
- [54] W. E. Lamb and R. C. Retherford, Fine structure of the hydrogen atom by a microwave method, *Phys. Rev.* **72**, 241 (1947).
- [55] H. A. Bethe, The electromagnetic shift of energy levels, *Phys. Rev.* **72**, 339 (1947).
- [56] L. Lehtovaara, J. Toivanen, and J. Eloranta, Solution of time-independent schrödinger equation by the imaginary time propagation method, *J. Comput. Phys.* **221**, 148 (2007).
- [57] P. Bader, S. Blanes, and F. Casas, Solving the schrödinger eigenvalue problem by the imaginary time propagation technique using splitting methods with complex coefficients, *J. Chem. Phys.* **139**, 124117 (2013).
- [58] Note that the maximum pulse envelope of  $A(t_{\max}) = 0.5$  a.u. translates to a Keldysh parameter of about  $\gamma = 180$ . The length of the envelope  $\tau = 10.0$  a.u. [full width at half maximum (FWHM)] is chosen short in order to reflect the short coherence time of self-amplified spontaneous emission FEL pulses and thus the narrow temporal window available for XNLC.
- [59] Note that, unfortunately, we cannot compare this result directly to the findings of Ref. [25], as the latter employs an ambiguous unit for its presentation of the DDSCS. In particular, one finds a DDSCS formulated akin to a linear scenario  $[r_0^2 \text{ eV}^{-1} \text{ sr}^{-1}]$ , whereas conventionally the nonlinear DDSCS would feature units  $[r_0^4 t_0 \text{ eV}^{-1} \text{ sr}^{-1}]$ . In order not to misrepresent the findings of Ref. [25], we have approached the authors for clarification. As we have not received any response, however, we abstain from comparing their data altogether.
- [60] Note that we employ a more intense Gaussian pulse for the simulations in Secs. III B and III C with  $A(t_{\max}) = 20.0$  a.u. Moreover, we use shorter pulses [ $\tau = 1.0$  a.u.(FWHM)], in accord with the coherence properties of SASE FELs at shorter wavelength.
- [61] S.-K. Son and R. Santra, XATOM, CFEL, DESY, Hamburg, Germany, 2011, <http://www.desy.de/~xraypac/xatom.html>.
- [62] Note that we employ NVIDIA Tesla K20m GPUs in single-card configuration.
- [63] C. W. McCurdy, M. Baertschy, and T. N. Rescigno, Solving the three-body coulomb breakup problem using exterior complex scaling, *J. Phys. B* **37**, R137 (2004).
- [64] J. C. Light, I. P. Hamilton, and J. V. Lill, Generalized discrete variable approximation in quantum mechanics, *J. Chem. Phys.* **82**, 1400 (1985).
- [65] J. C. Light and T. Carrington, Discrete-variable representations and their utilization, in *Advances in Chemical Physics* (John Wiley & Sons, New York, 2007), pp. 263–310.
- [66] S. Pabst, A. Sytcheva, O. Geffert, and R. Santra, Stability of the time-dependent configuration-interaction-singles method in the attosecond and strong-field regimes: A study of basis sets and absorption methods, *Phys. Rev. A* **94**, 033421 (2016).
- [67] N. Rohringer, A. Gordon, and R. Santra, Configuration-interaction-based time-dependent orbital approach for *ab initio* treatment of electronic dynamics in a strong optical laser field, *Phys. Rev. A* **74**, 043420 (2006).
- [68] H. Bachau, M. Dondera, and V. Florescu, Stimulated compton scattering of soft x-ray radiation by hydrogen, *J. Mod. Opt.* **63**, 402 (2016).
- [69] R. Kosloff and D. Kosloff, Absorbing boundaries for wave propagation problems, *J. Comput. Phys.* **63**, 363 (1986).
- [70] A. Goldberg and B. W. Shore, Modelling laser ionisation, *J. Phys. B* **11**, 3339 (1978).
- [71] C. Leforestier and R. E. Wyatt, Optical potential for laser induced dissociation, *J. Chem. Phys.* **78**, 2334 (1983).
- [72] G. Jolicard and E. J. Austin, Optical potential stabilisation method for predicting resonance levels, *Chem. Phys. Lett.* **121**, 106 (1985).
- [73] U. V. Riss and H.-D. Meyer, Calculation of resonance energies and widths using the complex absorbing potential method, *J. Phys. B* **26**, 4503 (1993).
- [74] R. Santra and L. S. Cederbaum, Non-hermitian electronic theory and applications to clusters, *Phys. Rep.* **368**, 1 (2002).
- [75] U. V. Riss and H.-D. Meyer, Reflection-free complex absorbing potentials, *J. Phys. B* **28**, 1475 (1995).
- [76] U. V. Riss and H.-D. Meyer, Investigation on the reflection and transmission properties of complex absorbing potentials, *J. Chem. Phys.* **105**, 1409 (1996).
- [77] U. V. Riss and H.-D. Meyer, The transformative complex absorbing potential method: a bridge between complex absorbing potentials and smooth exterior scaling, *J. Phys. B* **31**, 2279 (1998).
- [78] Note that for improved results, the integration of  $\partial_t \delta\rho_{i11}^{\text{phot}}(t)$  should be restricted to a temporal window around the peak of ejected electronic flux.
- [79] Note that XATOM is based on the same HFS approach for the noninteracting system as is our model, thus providing a sensible basis for comparison.
- [80] L. J. P. Ament, M. van Veenendaal, T. P. Devereaux, J. P. Hill, and J. van den Brink, Resonant inelastic x-ray scattering

- studies of elementary excitations, *Rev. Mod. Phys.* **83**, 705 (2011).
- [81] Note with respect to Fig. 6 that we have shifted the XATOM result prior to the comparison, in order to adjust for a slight difference in the respective HFS ionization potentials ( $\Delta IP = 0.0055$  a.u.  $\approx 0.15$  eV).
- [82] E. G. Drukarev, A. I. Mikhailov, and I. A. Mikhailov, Low-energy  $k$ -shell compton scattering, *Phys. Rev. A* **82**, 023404 (2010).
- [83] Note that the extent of nondipole effects in the light-matter coupling is in fact controlled by a convergence parameter, which determines the maximal angular momentum difference ( $l_{\text{cpl}}$ ) bridged by  $\hat{H}_{\text{int}}$ . To this end, any factor of  $e^{i\mathbf{k}\cdot\mathbf{r}}$  occurring in Eqs. (21)–(24) is expanded as  $4\pi \sum_{l=0}^{l_{\text{cpl}}} \sum_{m=-l}^l i^l j_l(kr) Y_{lm}^*(\Omega_{\mathbf{k}}) Y_{lm}(\Omega_{\mathbf{r}})$  up to  $l_{\text{cpl}}$  (cf. Ref. [84]).
- [84] D. A. Varshalovich, A. N. Moskalev, and V. K. Khersonskii, *Quantum Theory of Angular Momentum* (World Scientific, Singapore, 1988).